Thermal Decomposition of CF_3 and the Reaction of $CF_2 + OH \rightarrow CF_2O + H$

N. K. Srinivasan, M.-C. Su,† J. V. Michael,* A. W. Jasper,‡ S. J. Klippenstein,* and L. B. Harding*

Chemical Sciences and Engineering Division, Argonne National Laboratory, Argonne, Illinois 60439

Received: August 7, 2007; In Final Form: September 25, 2007

The reflected shock tube technique with multipass absorption spectrometric detection (at a total path length of ∼1.75 m) of OH-radicals at 308 nm has been used to study the dissociation of CF_3-radicals [$CF_3 + Kr \rightarrow CF_2 + F + Kr$ (a)] between 1803 and 2204 K at three pressures between ∼230 and 680 Torr. The OH-radical concentration buildup resulted from the fast reaction $F + H_2O \rightarrow OH + HF$ (b). Hence, OH is a marker for F-atoms. To extract rate constants for reaction (a), the [OH] profiles were modeled with a chemical mechanism. The initial rise in [OH] was mostly sensitive to reactions (a) and (b), but the long time values were additionally affected by $CF_2 + OH \rightarrow CF_2O + H$ (c). Over the experimental temperature range, rate constants for (a) and (c) were determined from the mechanistic fits to be $k_{CF_3+Kr} = 4.61 \times 10^{-9} \exp(-30020\ K/T)$ and $k_{CF_2+OH} = (1.6 \pm 0.6) \times 10^{-10}$, both in units of cm^3 $molecule^{-1}$ s^{-1}. Reaction (a), its reverse recombination reaction reaction (−a), and reaction (c) are also studied theoretically. Reactions (c) and (−a) are studied with direct CASPT2 variable reaction coordinate transition state theory. A master equation analysis for reaction (a) incorporating the ab initio determined reactive flux for reaction (−a) suggests that this reaction is close to but not quite in the low-pressure limit for the pressures studied experimentally. In contrast, reaction (c) is predicted to be in the high-pressure limit due to the high exothermicity of the products. A comparison with past and present experimental results demonstrates good agreement between the theoretical predictions and the present data for both (a) and (c).

Introduction

The reactions of CF_3 radicals play an important role in the flame retardant properties of halons, particularly CF_3Br.[1−3] Because the high-temperature reactions involved in the incineration of fluorine containing compounds are not well-known, earlier studies from this laboratory on the bimolecular destruction rates of CF_3H by H and its reverse, $CF_3 + H_2$,[4] and also CF_3H by OH and its reverse, $CF_3 + H_2O$,[5] were carried out. In both studies, the CF_3 destruction rate at $T > 1900$ K by atom and/or radical attack is always in competition with destruction due to thermal decomposition, and this realization has motivated the present study. There is only one prior study on

$$CF_3 + Kr \rightarrow CF_2 + F + Kr \qquad (1)$$

by Modica and Sillers[6] who used the shock tube time-of-flight mass spectrometric technique to measure the extent of reaction. Because relatively large concentrations of starting materials were necessary with this type of experiment, k_1 was determined by secondary product formation through an assumed mechanism. In contrast, in the present work, H_2O was added to the reaction mixture containing the source of CF_3-radicals, CF_3I. OH-radicals were then observed as a result of the fast subsequent reaction of F-atoms from (1) with H_2O.[7] The method involves measuring absolute [OH] temporal profiles and fitting a detailed mechanism to simulate the results. During the course of this work we were able to estimate experimental rate constants for the secondary reaction

$$CF_2 + OH \rightarrow CF_2O + H \qquad (2)$$

The experimental studies of reactions 1 and 2 are supplemented with high-level theoretical analyses. The high-pressure recombinations of F and OH with CF_2 (i.e., the high-pressure back-reaction of reaction 1 and reaction 2, respectively) are studied with direct CASPT2 variable reaction coordinate transition state theory.[8−10] The pressure dependence of the CF_3 decomposition is studied with master equation simulations.[11] These simulations indicate that reaction 1 is close to but not quite at the low-pressure limit for the temperatures and pressures studied here. The products from (2) are consistent with ab initio theoretical calculations which predict that the $CF_2O + H$ channel is highly exothermic. As a result, this reaction is expected to be independent of pressure for the temperature and pressure ranges studied here.

Experimental Section

Experiments. The present experiments were performed with the shock tube technique using OH-radical electronic absorption detection. We earlier described a long absorption path multipass optical system for OH-radical detection in the reflected shock regime[12] and used it to measure other high-temperature rate constants.[13−15] The method and the apparatus currently being used have been previously described[16,17] and only a brief description of the experiment will be presented here.

The shock tube is constructed from 304 stainless steel in three sections. The first 10.2 cm o.d. cylindrical section is separated from the He driver chamber by a 4 mil unscored 1100-H18

* Corresponding authors. J.V.M.: phone, (630) 252-3171; fax, (630) 252-4470; E-mail, jmichael@anl.gov.

† Special Term Appointment, Argonne. Permanent address: Department of Chemistry, Sonoma State University, 1801 E. Cotati Ave., Rohnert Park, CA 94928.

‡ Current address: Sandia National Laboratories, 7011 East Avenue, MS 9055, Livermore, CA 94551.

10.1021/jp076344u CCC: $40.75
Published on Web 12/07/2007

aluminum diaphragm. A 0.25 m transition section then connects the first and third sections. The third section is of rounded corner (radius, 1.71 cm) square design and is fabricated from flat stock (3 mm) with a mirror finish. Two flat fused silica windows (3.81 cm) with broadband antireflection (BB AR) coating for UV light are mounted on the tube across from one another at a distance of 6 cm from the end plate. The path length between windows is 8.745 cm. The incident shock velocity is measured with eight fast pressure transducers (PCB Piezotronics, Inc., Model 113A21) mounted along the third portion of the shock tube, and temperature and density in the reflected shock wave regime are calculated from this velocity and include corrections for boundary layer perturbations.[18−20] The tube is routinely pumped between experiments to $<10^{-8}$ Torr by an Edwards Vacuum Products Model CR100P packaged pumping system. A 4094C Nicolet digital oscilloscope was used to record the velocities and an LC334A LeCroy digital oscilloscope was used to record absorption signals.

The optical configuration consists of an OH resonance lamp, multipass reflectors, an interference filter at 308 nm, and a photomultiplier tube (1P28) all mounted external to the shock tube as described previously.[5,12−15] With this new configuration, we were able to obtain multiple passes, thereby amplifying the measured absorbances.

Gases. High-purity He (99.995%), used as the driver gas, was from AGA Gases. Scientific grade Kr (99.999%), the diluent gas in reactant mixtures, was from Spectra Gases, Inc. The ~10 ppm impurities (N_2, 2 ppm; O_2, 0.5 ppm; Ar, 2 ppm; CO_2, 0.5 ppm; H_2, 0.5 ppm; CH_4, 0.5 ppm; H_2O, 0.5 ppm; Xe, 5 ppm; CF_4, 0.5 ppm) are all either inert or are in sufficiently low concentration so as to not perturb OH-radical profiles. Distilled water, evaporated at 1 atm into ultrahigh-purity grade Ar (99.999%) from AGA Gases, was used at ~25 Torr pressure in the resonance lamp. Analytical grade CF_3I (97% from SynQuest Laboratories, Inc.) was further purified by bulb-to-bulb distillations with the middle third being retained. Triple distilled H_2O was also purified by bulb-to-bulb vacuum distillation retaining the middle third. Test gas mixtures were accurately prepared from pressure measurements using a Baratron capacitance manometer and were stored in an all glass vacuum line.

Theory: High-Pressure Recombination. *CF_2 + F*. The interaction of the F atom with CF_2 yields three nearly degenerate doublet electronic states at large separations. At infinite separation these states are split by the spin−orbit splitting of the F atom. At shorter separations one state correlates with the strongly bound ground state of the CF_3 radical, whereas the remaining two states are predicted to be repulsive. The recombination is presumed to occur only on the attractive state.

A contour diagram of the ground state interaction potential, as evaluated with multireference configuration interaction calculations, is provided in Figure 1. These multireference, singles and doubles configuration interaction (CAS+1+2+QC)[21,22] calculations employ a 7 electron 5 orbital complete active space consisting of the 3 p orbitals of F and the highest occupied and lowest unoccupied molecular orbitals (HOMO and LUMO) of CF_2. The calculations employ the aug-cc-pVDZ basis set of Dunning,[23] and include the Davidson correction for higher-order excitations.[24,25]

The interaction potential is weakly attractive for all orientations at long-range, but at about 5 au C···F separation (1 au = 0.529 Å), it becomes strongly repulsive for approach on the F side of the CF_2 molecule. Approach of the F atom from the opposite side yields a purely attractive potential with the plot

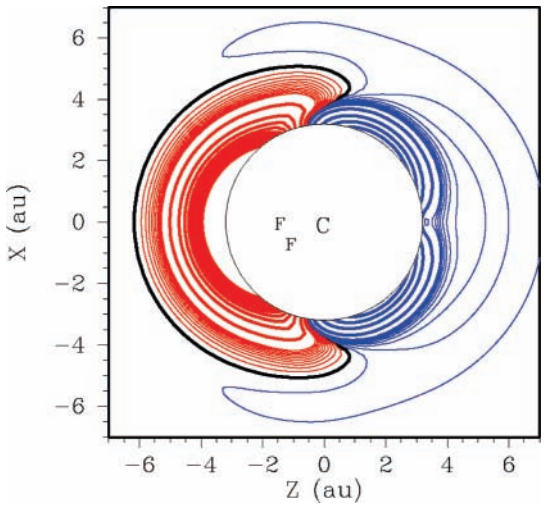

Figure 1. Two-dimensional contour plot of the CAS+1+2+QC/aug-cc-pvdz, F + CF_2, interaction potential. The CF_2 fragment is fixed at its equilibrium geometry in the *yz* plane with the symmetry axis coincident with the *z*-axis. The blue contours depict attractive interactions and the red repulsive. The thin contours have a contour increment of 0.5 kcal/mol and the thick contours have an increment of 10.0 kcal/mol.

again showing a sharp increase in the strength of the interactions at shorter separations (i. e., at C···F separations of about 4 au). The location of this sharp change in the strength of the interactions roughly correlates with the location of the transition state for the recombination reaction.

Direct CASPT2[26−28] variable reaction coordinate transition state theory[8−10] calculations were performed for both the cc-pVDZ[29] and the aug-cc-pVDZ basis set with the same 7 electron 5 orbital active space as in the CAS+1+2+QC exploration of the potential energy surface. The CAS orbitals were optimized for the average of the three lowest-energy electronic states. Alternatively, optimizing the orbitals in the CAS part of the calculation for the ground electronic state, yields predicted rate coefficients that are lower by up to 20%. A dynamical correction of 0.9 was incorporated, as suggested in our dynamical studies of radical plus H atom recombinations.[8]

The CASPT2, CAS+1+2+QC, and QCISD(T) calculations described here were performed with the MOLPRO quantum chemistry software.[30] Some underlying B3LYP geometry optimizations and frequency analyses were performed with the GAUSSIAN98 software.[31]

Several dividing surfaces were considered with fixed center of mass separations from 7 to 15 au with a grid spacing of 2 au. Multifaceted dividing surfaces were considered with pivot points displaced from the C atom by 0.5 or 1.0 au at 45° angles from the plane of the CF_2 fragment with pivot point separations of 3.5−4.5 au. At temperatures above ~300 K, the rate was found to be controlled by the short-range part of the potential, and the center of mass dividing surfaces contributed little to the overall rate coefficient.

The effect of including a geometry-dependent spin−orbit splitting correction was computed for the cc-pVDZ basis set using the methodology described in ref 10, and a temperature-dependent spin−orbit correction factor was obtained and is given by

$$C_{SO}(T) = k^{SO}_{cc-pVDZ}/k_{cc-pVDZ} \quad (3)$$

This correction factor increases from 0.7 to 0.94 as the temperature increases from 300 to 2500 K. The aug-cc-pVDZ

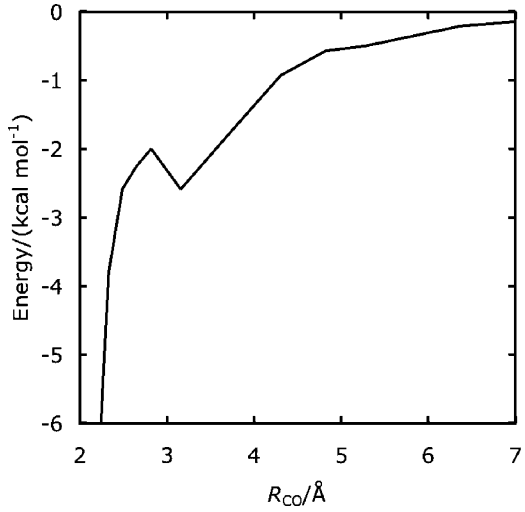

Figure 2. Minimum energy path for $CF_2 + OH$ association computed at the CASPT2/aug′-cc-pvdz level of theory and including a basis set correction potential.

result was corrected to include the effect of geometry-dependent spin−orbit splitting as follows:

$$k^{SO}_{aug-cc-pVDZ} = C_{SO} k_{aug-cc-pVDZ} \quad (4)$$

CF_2 + OH. The CF_2 + OH reaction is isoelectronic with the CF_2 + F reaction and thus has many features in common with it. At large separations there are now two nearly degenerate doublet electronic states corresponding to the two spin−orbit states of OH. At shorter separations, these two states split into an attractive ground state and a repulsive excited state. Again, the recombination is presumed to occur solely on the ground state.

Direct CASPT2 VRC-TST rate calculations were performed with the aug′-cc-pVDZ[32] basis set, which is similar to the aug-cc-pVDZ basis but neglects diffuse functions on the H atom. An approximation to results for the aug-cc-pVTZ basis set were obtained by incorporating a correction potential (CP) corresponding to the difference between CASPT2/aug-cc-pVTZ and CASPT2/aug′-cc-pVDZ calculations for the CH_3 + OH minimum energy path.[10] This correction potential yields an increase in the rate constant of ∼10−20%.

The active space for the direct CASPT2 calculations consisted of five electrons in four orbitals, with the active orbitals taken as the two Π orbitals of OH and the HOMO and LUMO of CF_2. The orbitals were optimized for the average energy of the two lowest-energy states, and two roots were requested using the RS2 algorithm in the CASPT2 calculation. Requesting one root from the RS2 algorithm resulted in rates 10−20% lower for 300−2500 K.

Several dividing surfaces were considered with fixed center of mass separations from 4.75 to 23 au on a variable grid and with fixed C−O distances from 4 to 6 au on a grid of ∼0.1 au. A dynamical correction of 0.85 was used on the basis of our direct dynamics simulations for $CH_3 + CH_3$.[9]

The minimum energy path (MEP) potential for the ground state, as obtained from the direct CASPT2 sampling in the VRC-TST rate calculations, is plotted in Figure 2. Notably, the MEP shows a distinct saddle point at a CO separation of about 3 Å. This saddle point arises as OH reorients from its optimal long-range (dipole−dipole) van der Waals orientation to that necessary for chemical bond formation. Although this inner saddle point is significantly below reactants, it still dominates the

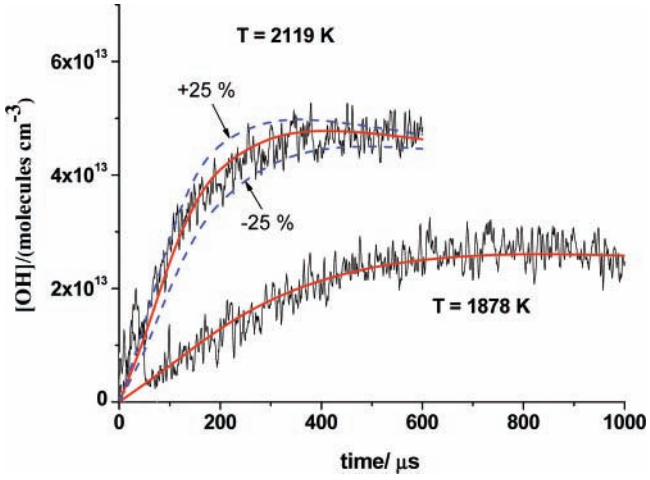

Figure 3. Two [OH] temporal profiles measured at high and low *T*. Solid lines: fits with the full reaction mechanism listed in Table 1 with final fitted values for k_{20} and k_{17} (see text). Dashed lines: fits with k_{20} and k_{17} varied by ±25%. The conditions for the high-*T* profile are $P_1 = 10.91$ Torr and $M_s = 2.941$, $T_5 = 2119$ K, $\rho_5 = 2.403 \times 10^{18}$ molecules cm^{-3}, $[CF_3I]_0 = 7.276 \times 10^{13}$ molecules cm^{-3}, and $[H_2O]_0 = 2.345 \times 10^{15}$ molecules cm^{-3}. The low-*T* conditions are $P_1 = 10.87$ Torr and $M_s = 2.766$, $T_5 = 1878$ K, $\rho_5 = 2.295 \times 10^{18}$ molecules cm^{-3}, $[CF_3I]_0 = 6.950 \times 10^{13}$ molecules cm^{-3}, and $[H_2O]_0 = 2.240 \times 10^{15}$ molecules cm^{-3}.

kinetics for room temperature and higher. Thus, we have performed a higher-level quantum chemical analysis of this saddle point. In particular, the saddle point geometry was located at the CASPT2/aug-cc-pVDZ level of theory, and a complete basis set (CBS) estimated QCISD(T) energy was obtained by extrapolating from energies obtained using the cc-pVTZ and cc-pVQZ basis sets.[10] The resulting electronic energy (−1.63 kcal/mol relative to CF_2 + OH) is 0.4 kcal/mol higher than the local maximum along the minimum energy curve obtained in the VRC-TST calculations and shown in Figure 2. Related large basis set CASPT2 calculations yield a similar energy. Thus, the final dynamically corrected VRC-TST rate coefficient was corrected with the corresponding Boltzmann factor, i.e., by exp(−*E*/*kT*), with $E = 0.4$ kcal/mol.

The MEP plot suggests that there should be both a long-range transition state, providing a bottleneck to the formation of the van der Waals complex, and a short-range bottleneck corresponding to chemical bond formation. For all but very low (∼100 K) temperatures, the canonical variational transition states were found to be located at small fragment separations (4.1−4.8 au), i.e., near the saddle point. Nevertheless, the two transition states should act in series, and their consideration within a unified statistical theory (UST)[10,33] model might lead to a significant reduction in the predicted rate coefficient. However, implementation of the UST model predicts a lowering of the rate by only 5% for room temperature and higher. This dominance of the inner transition state region also suggests that it is reasonable to neglect the effect of spin−orbit splitting for this reaction.

Theory: Pressure Dependence. The decomposition of CF_3 is a simple dissociation yielding CF_2 + F. The pressure dependence of this dissociation process was studied with master equation simulations as described in ref 10. The rovibrational properties of the reactants and products were determined with B3LYP/6-311++G(d,p) evaluations. The direct VRC-TST calculations described above provided the transition state microcanonical/J-resolved partition functions. Complete basis set QCISD(T) calculations performed at the

TABLE 1: Mechanism for Fitting [OH] Profiles

1	$CF_3I + Kr \rightarrow CF_3 + I + Kr$	$k_1 = 2.86 \times 10^{-9} \exp(-15943\ K/T)$	34
2	$H + O_2 \rightarrow OH + O$	$k_2 = 1.62 \times 10^{-10} \exp(-7474\ K/T)$	35
3	$OH + O \rightarrow O_2 + H$	$k_3 = 5.42 \times 10^{-13} T^{0.375} \exp(950\ K/T)$	16, 36, 37
4	$O + H_2 \rightarrow OH + H$	$k_4 = 8.44 \times 10^{-20} T^{2.67} \exp(-3167\ K/T)$	16
5	$OH + H \rightarrow H_2 + O$	$k_5 = 3.78 \times 10^{-20} T^{2.67} \exp(-2393\ K/T)$	16, 36, 37
6	$OH + H_2 \rightarrow H_2O + H$	$k_6 = 3.56 \times 10^{-16} T^{1.52} \exp(-1736\ K/T)$	38
7	$H_2O + H \rightarrow OH + H_2$	$k_7 = 1.56 \times 10^{-15} T^{1.52} \exp(-9083\ K/T)$	16, 36, 37
8	$OH + OH \rightarrow O + H_2O$	$k_8 = 7.19 \times 10^{-21} T^{2.7} \exp(917\ K/T)$	16, 36, 37, 39
9	$O + H_2O \rightarrow OH + OH$	$k_9 = 7.48 \times 10^{-20} T^{2.7} \exp(-7323\ K/T)$	16, 36, 37
10	$HO_2 + Kr \rightarrow H + O_2 + Kr$	$k_{10} = 7.614 \times 10^{-10} \exp(-22520\ K/T)$	40
11	$HO_2 + OH \rightarrow H_2O + O_2$	$k_{11} = 2.35 \times 10^{-10} T^{-0.21} \exp(56\ K/T)$	41
12	$CF_3 + OH \rightarrow CF_2O + HF$	$k_{12} = 2.42 \times 10^{-11} T^{-0.065} \exp(134\ K/T)$	5
13	$CF_3H + O \rightarrow CF_3 + OH$	$k_{13} = 3.69 \times 10^{-18} T^{2.36} \exp(-7294\ K/T)$	42
14	$CF_3H + OH \rightarrow CF_3 + H_2O$	$k_{14} = 9.7 \times 10^{-12} \exp(-4398\ K/T)$	5
15	$CF_3 + H_2O \rightarrow CF_3H + OH$	$k_{15} = k_{14} \times (4.125 \times 10^{-12} T^3 - 3.29 \times 10^{-9} T^2 - 1.55 \times 10^{-6} T + 1.381 \times 10^{-3})$	5, 43
16	$CF_3H \rightarrow CF_2 + HF$	$k_{16}(\rho,T)$ is interpolated from Figure 5 in ref 44	44
17	$CF_2 + OH \rightarrow CF_2O + H$	k_{17} see text	
18	$CF_2 + H \rightarrow CF + HF$	$k_{18} = 6.61 \times 10^{-11} \exp(-2285\ K/T)$	45
19	$OH + CF \rightarrow CO + HF$	$k_{19} = 1 \times 10^{-10}$	estimated
20	$CF_3 + Kr \rightarrow CF_2 + F + Kr$	k_{20} see text	
21	$F + H_2O \rightarrow OH + HF$	$k_{21} = 1.45 \times 10^{-11}$	7
22	$CF_3 + H \rightarrow CF_2 + HF$	$k_{22} = 8.86 \times 10^{-11}$	46
23	$CF_3 + O \rightarrow CF_2O + F$	$k_{23} = 2.55 \times 10^{-11}$	46
24	$CF_2 + O \rightarrow CO + 2F$	$k_{24} = 4.07 \times 10^{-11}$	45
25	$CF_3 + CF_2 \rightarrow C_2F_4 + F$	$k_{25} = 1.5 \times 10^{-12}$, geometric mean of self-combinations	4, 47

[a] All rate constants are in cm^3 molecule^{-1} s^{-1} except for 16, which is in s^{-1}.

B3LYP/6-311++G(d,p) optimized geometries yield a 0 K dissociation energy of 84.2 kcal/mol. This dissociation energy and the B3LYP rovibrational properties are employed in the computation of equilibrium constants. The energy transfer was represented with the temperature-dependent exponential down form

$$\langle \Delta E_d \rangle = \alpha \left(\frac{T}{300\ \mathrm{K}} \right)^{\gamma} \quad (5)$$

with $\alpha = 200\ cm^{-1}$ and $\gamma = 0.85$, chosen in analogy with related studies and to fit the experimental data. Lennard-Jones collision rates were employed.

For the $CF_2 + OH$ reaction, the $CF_2O + H$ product channel is highly exothermic (55.0 kcal/mol at the QCISD(T)/CBS level). With such a large exothermicity there should be essentially no collisional stabilization of the CF_2OH complex (69.4 kcal/mol exothermic) except perhaps at very low temperature and extraordinarily high pressures. For the temperatures and pressures of interest here it is reasonable to assume that the rate coefficient is pressure independent. The geometries and rovibrational properties of the reactants and products for both reactions are available as Supporting Information.

Results

The experiments were performed using 20 optical passes (path length = 1.75 m). The OH temporal concentration increase was determined from measured absorbance, $(ABS)_t = \ln[I_0/I_t] = [OH]_t l \sigma_{OH}$, using a previously measured absorption cross-section at 308 nm ($\sigma_{OH} = (4.516 - 1.18 \times 10^{-3} T) \times 10^{-17}$ cm^2 molecule^{-1}).[14] Experiments were performed with ~30−60 ppm CF_3I and ~1000 ppm H_2O between 1803 and 2204 K. The pressure range was ~230−680 Torr. Typical results at 1878 and 2119 K are shown in Figure 3. Note that OH formation appears to follow a first-order buildup rate law. Hence, we first determined buildup constants, k_{first}, and then estimated bimolecular rate constants as $k_1 = k_{first}/[M]$ to be used as starting values in simulations with the mechanism of Table 1. However, to obtain the best fits, k_1 values (k_{20} in the table) had to be slightly varied from the initial estimate, and the solid lines shown in Figure 3 are typical simulations with the final fitted value for k_1. Figures 4 and 5 show normalized sensitivity analyses (i.e., $S = (d[OH]/dk_i)(k_i/[OH])$) corresponding to Figure 3, and it is clear that the early time profile is dominated by reaction 1. Other reactions, shown as insets in the figures, do contribute to long time [OH], nearly counterbalancing one another, giving the apparent first-order behavior. A majority of the rate constants for these other reactions have been estimated and/or measured as indicated in Table 1; however, to predict the longer time values, the $CF_2 + OH$ rate constant, k_2 (k_{17} in the table) also had to be adjusted. Note that the reaction $CF_3 + OH$ (k_{12} in the table) shows substantial sensitivity. This rate constant was recently measured in this laboratory and shown to be in excellent agreement with theoretical calculations[5] and therefore cannot be varied in the simulations. Hence, in large measure, the profiles are mostly dominated by CF_3 decomposition and $CF_2 + OH$. The dashed lines shown in Figure 3 are calculated with both rate constants varied by ±25%, respectively.

Rate constant values for reaction 1 from 28 experiments are listed in Table 2 along with the conditions for each experiment. In all cases, reaction 1 dominates the initial time profiles, and therefore the derived rate constants are nearly direct. Note that the $[H_2O]_0$ in this work is substantially less than in earlier work from this laboratory[5] on $CF_3 + H_2O \rightarrow CF_3H + OH$, which was carried out at lower T where CF_3 dissociation is negligible. In the present case, OH can only be formed by the fast reaction, $F + H_2O \rightarrow OH + HF$, thereby serving as a marker for F-atom formation. To reproduce the long time profiles, rate constant values for reaction 2 (k_{17} in Table 1) ranging from 0.8×10^{-11} to 2.0×10^{-11} with the average being $k_{17} = (1.6 \pm 0.6) \times 10^{-11}$ cm^3 molecule^{-1} s^{-1} were required for the entire set.

The rate constants for reaction 1 from Table 2 are plotted in Figure 6 in Arrhenius form. Within the experimental scatter of the data, no pressure effects are indicated between ~265 to ~650 Torr, suggesting that the data are near the low-pressure limit. The line shown in the figure is then a linear-least-squares line including all data points given by

$$\log k_1 = (-8.34 \pm 0.31) - (13038 \pm 591\ \mathrm{K})/T \quad (6)$$

where k_1 is in cm^3 molecule^{-1} s^{-1}. Equation 6 is valid over the

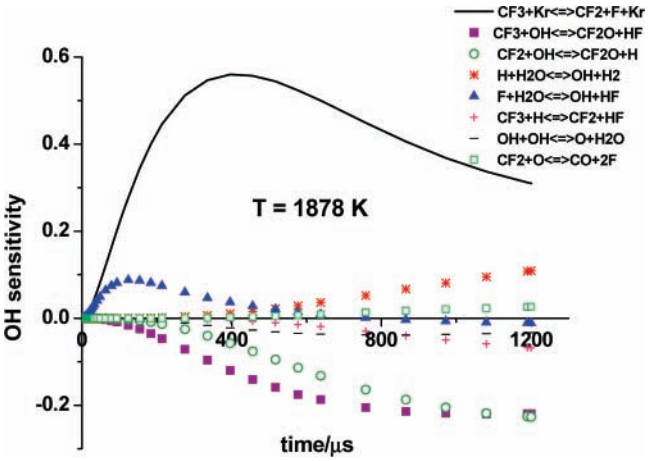

Figure 4. OH-radical sensitivity analysis for the 1878 K profile shown in Figure 3 using the full reaction mechanism. The eight most sensitive reactions are shown as the inset.

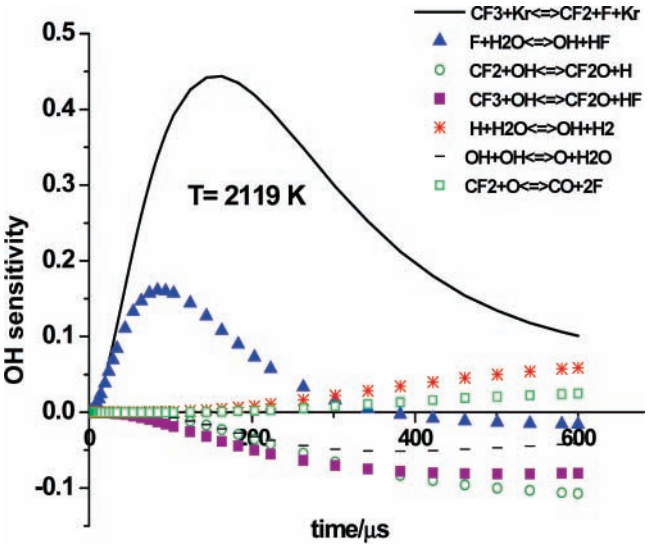

Figure 5. OH-radical sensitivity analysis for the 2119 K profile shown in Figure 3 using the full reaction mechanism. The seven most sensitive reactions are shown as the inset.

T range 1803−2204 K. At the one standard deviation level, the data points are within ±20% of the line calculated from (6).

Discussion

Experiments. As far as we are aware, there is only one earlier experimental study on the thermal decomposition of CF_3 by Modica and Sillers.[6] Their value is 2−2.5 times larger than eq 6 over the present temperature range at similar pressures. There are reports of rate constants for reaction 2 (i. e., reaction 17 in Table 1), the earliest being that of Biordi et al.[48] who, from molecular beam-mass spectrometric flame experiments, suggest values between 0.83×10^{-11} and 4.98×10^{-11} cm^3 molecule^{-1} s^{-1} over the temperature range 1090−1700 K. Other workers have also adopted values within this range.[47,49,50] The present value, $k_2 = (1.6 \pm 0.6) \times 10^{-11}$ cm^3 molecule^{-1} s^{-1} (error is at the one standard deviation level), is between the upper and lower limits, as shown in Figure 7. In the section to follow, reaction 1 ((20) in Table 1) and reaction 2 will both be theoretically addressed and compared to experiment.

Theory. The dynamically corrected VRC-TST predictions for the high-pressure limit recombination rate coefficients for the $CF_2 + F$ and $CF_2 + OH$ reactions are illustrated in Figure 7. These rate coefficients are well reproduced by the modified

TABLE 2: High-Temperature Rate Data for $CF_3 + Kr \rightarrow CF_2 + F + Kr$

P_1/Torr	M_s[a]	$\rho_5/(10^{18}$ cm$^{-3})$[b]	T_5/K	k_1[c]
$X_{CF_3I} = 3.134 \times 10^{-5}$		$X_{H_2O} = 1.007 \times 10^{-3}$		
15.95	2.736	3.303	1828	2.95(−16)[d]
15.93	2.797	3.368	1896	5.70(−16)
15.95	2.870	3.438	1987	1.48(−15)
15.92	2.771	3.331	1871	5.20(−16)
15.90	2.722	3.269	1818	2.98(−16)
$X_{CF_3I} = 5.965 \times 10^{-5}$		$X_{H_2O} = 1.948 \times 10^{-3}$		
5.93	2.760	1.243	1880	6.42(−16)
5.92	2.878	1.289	2026	2.20(−15)
5.95	2.779	1.255	1905	9.86(−16)
5.90	2.746	1.236	1857	5.14(−16)
5.94	2.703	1.227	1803	2.86(−16)
5.97	2.910	1.311	2067	2.14(−15)
5.97	2.941	1.317	2116	3.79(−15)
5.96	3.011	1.343	2204	6.08(−15)
5.96	2.936	1.318	2103	2.23(−15)
5.92	2.850	1.288	1977	1.39(−15)
5.88	2.823	1.269	1941	1.22(−15)
$X_{CF_3I} = 3.028 \times 10^{-5}$		$X_{H_2O} = 9.758 \times 10^{-4}$		
15.97	2.754	3.313	1856	4.67(−16)
15.90	2.827	3.377	1940	7.09(−16)
15.94	2.766	3.330	1865	3.12(−16)
10.87	2.766	2.295	1878	6.06(−16)
10.91	2.850	2.352	1991	1.12(−15)
10.90	2.817	2.328	1948	9.21(−16)
10.88	2.812	2.320	1942	8.67(−16)
10.86	2.918	2.386	2081	2.04(−15)
10.91	2.941	2.403	2119	2.75(−15)
10.88	2.772	2.293	1892	4.63(−16)
10.89	2.738	2.272	1849	3.66(−16)
10.97	2.737	2.287	1847	3.59(−16)

[a] The error in measuring the Mach number, M_s, is typically 0.5−1.0% at the one standard deviation level. [b] Quantities with the subscript 5 refer to the thermodynamic state of the gas in the reflected shock region. [c] Rate constants in units cm^3 molecule^{-1} s^{-1}. [d] Parentheses denotes the power of 10.

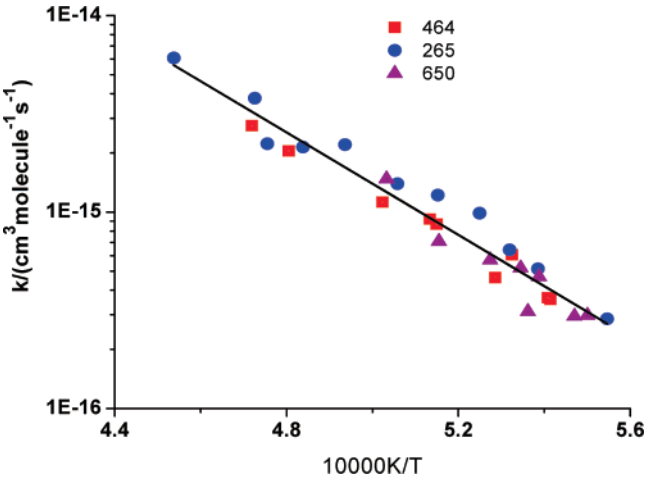

Figure 6. Arrhenius plot of the data for k_{20} from Table 2 (1803−2204 K): [●] 265 Torr; [■] 464 Torr; [▲] 650 Torr. The solid thick line is a linear-least-squares fit of the data (eq 6) over the entire T and P ranges.

Arrhenius expressions $k_{-1}^{\infty} = 1.265 \times 10^{-11}(T/298\text{ K})^{0.4717}$ exp(347.1 K/T) and $k_2^{\infty} = 4.508 \times 10^{-12}(T/298\text{ K})^{0.7539}$ exp(−454 K/T) cm^3 molecule^{-1} s^{-1} for (1) and (2), respectively, over the 300−2500 K temperature range. The $CF_2 + OH$ rate is somewhat lower than the $CF_2 + F$ rate, due to the increased steric reduction arising from the two additional transitional modes.

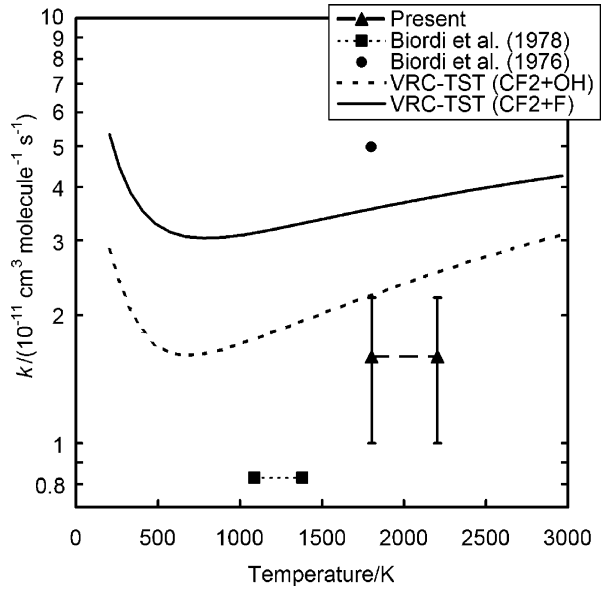

Figure 7. Present [▲] and previous [■, ●] measured rate coefficients for $CF_2 + OH$. Also shown are the present predicted VRC-TST rate coefficients for $CF_2 + OH$ (dotted line) and $CF_2 + F$ (solid line).

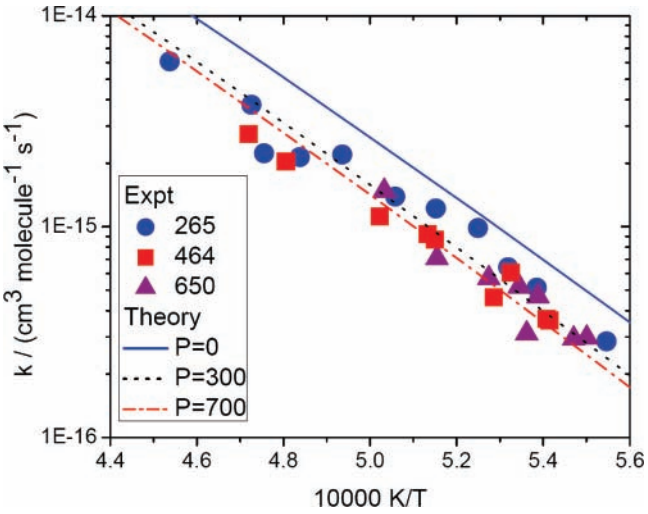

Figure 8. Plot of the predicted temperature dependence of the low-pressure rate coefficients for reaction 1, CF_3 dissociation. The data points are from Table 2 and are the same as shown in Figure 6.

The theoretical predictions for the temperature dependence of the CF_3 second-order dissociation rate constants are plotted in Figure 8. The theoretical predictions and experimental observations (230−680 Torr) are seen to be in good agreement, with the only adjustable parameter being the value for $\langle \Delta E_d \rangle$, eq 5. The experimental measurements at low and high densities correlate with the 300 and 700 Torr calculations, respectively. The theoretical predictions for the collisionless limit are also shown as an illustration of the moderate deviations from the lower-pressure predictions. In fact, even at 1 Torr, theory predicts that the deviations from the low-pressure limit are still significant (i.e., >20%) even though such pressure dependence is not revealed by the experiments due to the data scatter. The collisionless limit rate constants are well represented by the expression, $k_1^0 = 3.95(T/298)^{-6.362} \exp(-45649\ \mathrm{K}/T)$ cm^3 molecule^{-1} s^{-1}, for the 1300−2500 K range. The high-pressure limit dissociation rate constants are well reproduced by the expression $k_1^\infty = 1.27 \times 10^{16}(T/298)^{-0.868} \exp(-43186\ \mathrm{K}/T)$ s^{-1}, for the 1300−2500 K range, and therefore $K_1 = k_1^\infty/k_{-1}^\infty$. Also, the pressure dependence of the rate constants can be reproduced with the Troe form employing a temperature-independent F_{cent} of 0.27, again for the 1300−2500 K range.

The theoretical predictions for k_2 at 1803 and 2204 K are 2.25 and 2.50, both in units of 10^{-11} cm^3 molecule^{-1} s^{-1}, to be compared to the experimental value of $k_2 = (1.6 \pm 0.6) \times 10^{-11}$ cm^3 molecule^{-1} s^{-1}. Due to the substantial experimental scatter and to the substantial uncertainties in theoretically calculating these rate constants, we consider this discrepancy to be minor.

Acknowledgment. This work was supported by the U.S. Department of Energy, Office of Basic Energy Sciences, Division of Chemical Sciences, Geosciences and Biosciences under Contract No. DE-AC02-06CH11357.

Supporting Information Available: Geometries and rovibrational properties of the reactants and products. This material is available free of charge via the Internet at http://pubs.acs.org.

References and Notes

(1) Babushok, V.; Burgess, D. R. F.; Miziolek, A.; Tsang, W. In *Halon Replacements: Technology and Science*; Miziolek, A., Tsang, W., Eds.; American Chemical Society: Washington, DC, 1995; Vol. 611, p 275.
(2) Andersen, S. O.; Metchis, K. L.; Rubenstein, R. In *Halon Replacements: Technology and Science*; Miziolek, A., Tsang, W., Eds.; American Chemical Society: Washington, DC, 1995; Vol. 611, p 8.
(3) Babushok, V.; Noto, T.; Burgess, D. R. F.; Hamins, A.; Tsang, W. *Combust. Flame* **1996**, *107*, 351.
(4) Hranisavljevic, J.; Michael, J. V. *J. Phys. Chem.* **1998**, *102*, 7668.
(5) Srinivasan, N. K.; Su, M.-C.; Michael, J. V.; Klippenstein, S. J.; Harding, L. B. *J. Phys. Chem. A* **2007**, *111*, 6822.
(6) Modica, A. P.; Sillers, S. J. *J. Chem. Phys.* **1968**, *48*, 3283.
(7) Stevens, P. S.; Brune, W. H.; Anderson, J. G. *J. Phys. Chem.* **1989**, *93*, 4068.
(8) Harding, L. B.; Georgievskii, Y.; Klippenstein, S. J. *J. Phys. Chem. A* **2005**, *109*, 4646.
(9) Klippenstein, S. J.; Georgievskii, Y.; Harding, L. B. *Phys. Chem. Chem. Phys.* **2006**, *8*, 1133.
(10) Jasper, A. W.; Klippenstein, S. J.; Harding, L. B.; Ruscic, B. *J. Phys. Chem. A* **2007**, *111*, 3932.
(11) Miller, J. A.; Klippenstein, S. J. *J. Phys. Chem. A* **2006**, *110*, 10528.
(12) Su, M.-C.; Kumaran, S. S.; Lim, K. P.; Michael, J. V. *Rev. Sci. Instrum.* **1995**, *66*, 4649.
(13) Su, M.-C.; Kumaran, S. S.; Lim, K. P.; Michael, J. V.; Wagner, A. F.; Harding, L. B.; Fang, D.-C. *J. Phys. Chem. A* **2002**, *106*, 8261.
(14) Srinivasan, N. K.; Su, M.-C.; Sutherland, J. W.; Michael, J. V. *J. Phys. Chem. A* **2005**, *109*, 1857.
(15) Srinivasan, N. K.; Su, M.-C.; Sutherland, J. W.; Michael, J. V. *J. Phys. Chem. A* **2005**, *109*, 7902.
(16) Michael, J. V. *Prog. Energy Combust. Sci.* **1992**, *18*, 327.
(17) Michael, J. V. In *Advances in Chemical Kinetics and Dynamics*; Barker, J. R., Ed.; JAI: Greenwich, CT, 1992; Vol. I, pp 47−112, for original references.
(18) Michael, J. V.; Sutherland, J. W. *Int. J. Chem. Kinet.* **1986**, *18*, 409.
(19) Michael, J. V. *J. Chem. Phys.* **1989**, *90*, 189.
(20) Michael, J. V.; Fisher, J. R. In *Seventeenth International Symposium on Shock Waves and Shock Tubes*; Kim, Y. W., Ed.; AIP Conference Proceedings 208; American Institute of Physics: New York, 1990; pp 210−215.
(21) Werner, H.-J.; Knowles, P. J. *J. Chem. Phys.* **1988**, *89*, 5803.
(22) Knowles, P. J.; Werner, H.-J. *Chem. Phys. Lett.* **1988**, *145*, 514.
(23) Kendall, R. A.; Dunning, T. H., Jr.; Harrison, R. J. *J. Chem. Phys.* **1992**, *96*, 6796.
(24) Langhoff, S. R.; Davidson, E. R. *Int. J. Quantum Chem.* **1974**, *8*, 61.
(25) Silver, D. W.; Davidson, E. R. *Chem. Phys. Lett.* **1978**, *52*, 403.
(26) Werner, H.-J. *Mol. Phys.* **1996**, *89*, 645.
(27) Celani, P.; Werner, H.-J. *J. Chem. Phys.* **2000**, *112*, 5546.
(28) Celani, P.; Werner, H.-J. *J. Chem. Phys.* **2003**, *119*, 5044.
(29) Dunning, T. H., Jr. *J. Chem. Phys.* **1989**, *90*, 1007.
(30) MOLPRO is a package of ab initio programs written by Werner, H.-J.; Knowles, P. J. with contributions from Almlof, J.; Amos, R. D.; Berning, A.; Cooper, D. L.; Deegan, M. J. O.; Dobbyn, A. J.; Eckert, F.; Elbert, S. T.; Hampel, C.; Lindh, R.; Lloyd, A. W.; Meyer, W.; Nicklass, A.; Peterson, K.; Pitzer, R.; Stone, A. J.; Taylor, P. R.; Mura, M. E.; Pulay, P.; Schutz, M.; Stoll, H.; Thorsteinsson, T. The majority of calculations reported here were done with Version 2006.1.

(31) Frisch, M. J.; Trucks, G. W.; Schlegel, H. B.; Scuseria, G. E.; Robb, M. A.; Cheeseman, J. R.; Zakrzewski, V. G.; Petersson, G. A.; Montgomery, J. A., Jr.; Stratmann, R. E.; Burant, J. C.; Dapprich, S.; Millam, J. M.; Daniels, A. D.; Kudin, K. N.; Strain, M. C.; Farkas, O.; Tomasi, J.; Barone, V.; Cossi, M.; Cammi, R.; Mennucci, B.; Pomelli, C.; Adamo, C.; Clifford, S.; Ochterski, J.; Petersson, G. A.; Ayala, P. Y.; Cui, Q.; Morokuma, K.; Malick, D. K.; Rabuck, A. D.; Raghavachari, K.; Foresman, J. B.; Cioslowski, J.; Ortiz, J. V.; Stefanov, B. B.; Liu, G.; Liashenko, A.; Piskorz, P.; Komaroni, I.; Gomperts, R.; Martin, R. L.; Fox, D. J.; Keith, T. A.; Al-Laham, M. A.; Peng, C. Y.; Nanayakkara, A.; Gonzalez, C.; Challacombe, M.; Gill, P. M. W.; Johnson, B. G.; Chen, W.; Wong, M. W.; Andreas, J. L.; Head-Gordon, M.; Replogle, E. S.; Pople, J. A. *Gaussian 98*; Gaussian, Inc.: Pittsburgh, PA, 1998.

(32) DelBene, J. E. *J. Phys. Chem.* **1993**, *97*, 107.

(33) Miller, W. H. *J. Chem. Phys.* **1976**, *65*, 2216.

(34) Kumaran, S. S.; Su. M.-C.; Lim, K. P.; Michael, J. V. *Chem. Phys. Lett.* **1995**, *243*, 59.

(35) Du, H.; Hessler, J. P. *J. Chem. Phys.* **1992**, *96*, 1077.

(36) Ruscic, B.; Wagner, A. F.; Harding, L. B.; Asher, R. L.; Feller, D.; Dixon, D. A.; Peterson, K. A.; Song, Y.; Qian, X.; Ng, C. Y.; Liu, J.; Chen, W.; Schwenke, D. W. *J. Phys. Chem. A* **2002**, *106*, 2727.

(37) Herbon, J. T.; Hanson, R. K.; Golden, D. M.; Bowman, C. T. *Proc. Combust. Inst.* **2002**, *29*, 1201.

(38) Oldenborg, R. C.; Loge, G. W.; Harridine, D. M.; Winn, K. R. *J. Phys. Chem.* **1992**, *96*, 8426.

(39) Wooldridge, M. S.; Hanson, R. K.; Bowman, C. T. *Int. J. Chem. Kinet.* **1994**, *26*, 389.

(40) Michael, J. V.; Su, M.-C.; Sutherland, J. W.; Carroll, J. J.; Wagner, A. F. *J. Phys. Chem. A* **2002**, *106*, 5297.

(41) (a) Gonzalez, C.; Theisen, J.; Schlegel, H. B.; Hase, W. L.; Kaiser, E. W. *J. Phys. Chem.* **1992**, *96*, 1767. (b) Srinivasan, N. K.; Su, M.-C.; Sutherland, J. W.; Michael, J. V.; Ruscic, B. *J. Phys. Chem. A* **2006**, *110*, 6602.

(42) Fernandez, A.; Fontijn, A. *J. Phys. Chem. A* **2001**, *105*, 8196.

(43) Ruscic, B. Private communication of unpublished results obtained from Active Thermochemical Tables 1.25 and the Core (Argonne) Thermochemical Network 1.049 (2005) Tables.

(44) Schug, K. P.; Wagner, H. Gg.; Zabel, F. *Ber. Bunsen-Ges. Phys. Chem.* **1979**, *83*, 167.

(45) Yamamori, Y.; Takahashi, K.; Inomata, T. *J. Phys. Chem. A* **1999**, *103*, 8803.

(46) Takahashi, K.; Sekiuji, Y.; Yamamori, Y.; Inomata, T.; Yokoyama, K. *J. Phys. Chem. A* **1998**, *102*, 8339.

(47) Battin-Leclerc, F.; Smith, A. P.; Hayman, G. D.; Murrells, T. P. *J. Chem. Soc, Faraday Trans.* **1996**, *92*, 3305.

(48) Biordi, J. C.; Lazzara, C. P.; Papp, J. F. *J. Phys. Chem.* **1976**, *80*, 1042; *J. Phys. Chem.* **1978**, *82*, 125.

(49) Westbrook, C. K. *Combust. Sci. Technol.* **1983**, *34*, 201.

(50) Sanogo, O.; Delfau, J. L.; Akrich, R.; Vovelle, C. *Proc. Combust. Inst.* **1994**, *25*, 1489.